

Non-Schmid Effect on the Fracture Behavior of Tungsten

Zhijie Li ¹ and Yinan Cui ^{2,*} ¹ Institute of Nuclear and New Energy Technology, Tsinghua University, Beijing 100084, China² Applied Mechanics Laboratory, Department of Engineering Mechanics, School of Aerospace, Tsinghua University, Beijing 100084, China

* Correspondence: cyn@mail.tsinghua.edu.cn

Abstract: The fracture process of tungsten is dominated by the competition mechanism between the plastic deformation and the crack propagation near the crack tip. The non-Schmid (NS) effect, which considers the contribution of non-planar shear stress on the screw dislocation motion, is known to significantly influence the plastic deformation of tungsten at low and medium temperatures. However, how the NS effect influences the crack-tip plasticity and the fracture behavior of tungsten remains to be answered. In this work, the coupled crystal-plasticity and phase-field model (CP-PFM) was adopted to study the influence of the NS effect on the plastic deformation of un-notched tungsten and the fracture process of pre-notched tungsten at different temperatures. It was found that the lower the temperature, the more significant the NS effect on tungsten plasticity, which manifests in the lower yield stress and more unsymmetrical plastic deformation when the NS effect is considered. In contrast, the NS effect displayed the most obvious effect on the fracture behavior of pre-notched tungsten in the medium temperature regime, which manifested as higher fracture stress, a more significant crack-tip shielding effect, different fracture morphology, and lower crack propagation speed. The brittle fracture response at low temperature was not affected too much by the existence of the NS effect.

Keywords: fracture behavior; non-Schmid effect; dislocation motion; temperature; tungsten



Citation: Li, Z.; Cui, Y. Non-Schmid Effect on the Fracture Behavior of Tungsten. *Crystals* **2023**, *13*, 417. <https://doi.org/10.3390/cryst13030417>

Academic Editor: Ronald W. Armstrong

Received: 8 February 2023
Revised: 21 February 2023
Accepted: 23 February 2023
Published: 28 February 2023



Copyright: © 2023 by the authors. Licensee MDPI, Basel, Switzerland. This article is an open access article distributed under the terms and conditions of the Creative Commons Attribution (CC BY) license (<https://creativecommons.org/licenses/by/4.0/>).

1. Introduction

Due to its outstanding physical properties such as high melting temperature and great resistance to irradiation, tungsten is widely used in the electronics and energy industries. Tungsten generally exists in two major crystalline forms: α and β . Among them, α -tungsten has a body-centered cubic (BCC) structure and is the commonly existing stable form, while β -tungsten adopts a topologically close-packed cubic A15 structure containing eight atoms per unit cell and is a metastable phase widely observed in tungsten thin films [1,2], which was not considered in this work. The minimum working temperature of tungsten components is generally determined by the temperature of the brittle-to-ductile transition (BDT) [3,4]. Considering that the activation energy of the BDT process is close to the activation energy of the kink pair on screw dislocations, it is widely believed that the screw dislocation mobility dominates the BDT [5–9]. On the other hand, in tungsten, screw dislocation mobility also dominates the plastic deformation at low and medium temperatures. The non-planar core structure of screw dislocation leads to high Peierls stress and several special features of plastic deformation [10,11] such as the temperature and strain rate dependence and non-Schmid (NS) effect [12]. This raises a fundamental question as to how the NS effect influences the fracture behavior of tungsten, which remains to be answered.

The well-known Schmid law means that the dislocation motions at a given slip system is determined by the magnitude of the resolved shear stress, and non-glide components of the stress tensor have no influence on dislocation motion. However, in body-centered

cubic (BCC) metals, the non-planar core structure of screw dislocations make the non-glide stress components affect the dislocation motion, leading to the NS effect [11,13–16], manifested as tension/compression asymmetry, twinning/anti-twinning asymmetry, and strong loading orientation dependence, etc. Previous studies have demonstrated that the NS effect influences the yield stress, and promotes the deformation localization of irradiated tungsten and non-irradiated BCC metals [17–20]. Therefore, it is expected that the NS effect will influence the plastic deformation process around the crack tip and then influence the fracture behavior. However, very few studies have been reported, since it requires a model that is able to simultaneously consider the NS effect of tungsten plasticity and the fracture evolution process.

Only a few coupled models of dislocation-based plasticity (such as crystal plasticity (CP)) and fracture (such as phase field model (PFM) and cohesive zone model (CZM)) have been developed to study the fracture behavior of metals. Regarding the CP and CZM coupled model [21–23], the cohesive elements should first be embedded according to the a priori knowledge of the crack paths for the CZM [24]. This kind of model has limitations in handling the complex fracture behavior. In contrast, the CP-PFM coupled model has the inherent advantage in simulating complex crack behavior due to the use of PFM [25–29]. As a variational approach of fracture, PFM adopts the continuous damage variable to describe the discrete crack topology. PFM is derived from Griffith's theory and the first law of thermodynamics, and can capture the fracture process without the need to trace the fracture surface and the a priori knowledge of the crack path [30]. A few CP-PFM coupled models have been developed to predict the complex crack processes of the cleavage failure (or brittle fracture) [31] and the ductile fracture of metals [32,33]. However, in the above developed models, the phenomenological CP model is generally adopted to describe the plastic deformation, and the plastic strain rate is expressed as a function of resolved shear stress and critical stress, which does not directly consider the mobility and evolution of dislocation [34,35]. This kind of CP model cannot reproduce the NS effect of tungsten plasticity well.

To overcome this limitation, we recently developed a CP-PFM coupled model based on a unified thermodynamic framework [36] that directly considers the thermal activated kink-pair mechanism of the screw dislocation motion and the NS effect [20,37,38], and has been proven to be able to well capture the BDT of tungsten. Our previous work preliminarily demonstrated the significant influence of the NS effect on crack propagation by taking one result at 373 K as an example [36]. In the current work, systematic studies were carried out to address the NS effect on the brittle and ductile fracture behaviors of tungsten at different temperatures from the macroscopic and microscopic perspectives using our recently developed unique CP-PFM model. This study will lead to a new understanding of the correlation between screw the dislocation mobility and tungsten fracture behaviors.

2. Coupled Crystal-Plasticity and Phase-Field Model

In our previous work [36], the coupled crystal-plasticity and phase-field model (CP-PFM) was developed to simulate the fracture behavior of tungsten at different temperatures, which involves the evolution of the displacement, temperature, and discrete cracks. In the proposed CP-PFM model, the CP model was adopted to describe the plastic deformation at the macro scale based on the information of dislocation motion at the micro scale, thus accurately describing the special plastic features of tungsten including the temperature dependence and NS effect. The PFM model was used to describe the evolution of the discrete crack topology using the continuous damage variable. The detailed information of the CP-PFM model has been provided in our previous work [36]. In the following, only some key features of this model are briefly introduced.

In PFM, the discontinuous crack is approximately described by the dimensionless phase field variable d with a diffusive crack topology. When $d = 0$, the material is intact,

while $d = 1$ means that the crack is fully formed. The corresponding damage field evolution can be calculated as

$$\frac{G_c}{l_0} [d - l_0^2 \nabla^2 d] = 2(1 - d) (\Psi_+^{e0} + \Psi^{p,l}) \tag{1}$$

$$\Psi_+^{e0} = \begin{cases} \Psi_{e0}, & J \geq 1. \\ \Psi_{e0} - \frac{1}{2} K J^2, & J < 1. \end{cases} \tag{2}$$

$$\Psi^{e0} = \frac{1}{2} \mathbf{E}^e : \mathbf{C}^e : \mathbf{E}^e = \frac{1}{2} \mathbf{S}_0 : \mathbf{E}^e \tag{3}$$

$$\Psi^{p,l} = \frac{\epsilon}{2} \bar{\epsilon}^p - \bar{\epsilon}^{p,lock} \tag{4}$$

where G_c is the critical energy release rate, and l_0 is the character length parameter controlling the width of the diffusive crack. As l_0 approaches zero, the diffusive crack converges to the discrete crack. Ψ_+^{e0} is the tensile part of the elastic strain energy Ψ^{e0} ; K is the bulk modulus; J is the volumetric deformation; \mathbf{S}_0 is the second Piola–Kirchhoff stress without considering the material damage; \mathbf{C}^e and \mathbf{E}^e are the elasticity tensor and elastic Green strain, respectively. The penalty parameter ϵ is always set as a very large value to induce the ductile fracture when the equivalent plastic strain $\bar{\epsilon}^p$ reaches the critical value $\bar{\epsilon}^{p,lock}$ [39]. Ψ_+^{e0} and $\Psi^{p,l}$ are the driving energy of crack propagation and are calculated through the CP model, which will be described in the following.

In the CP model, the dislocation motion is the carrier of the plastic deformation. The plastic velocity gradient $\hat{\mathbf{L}}^p$ can be calculated as [11,13–16]

$$\hat{\mathbf{L}}^p = \sum_{\beta} \mathbf{P}_S^{\beta} \dot{\gamma}^{\beta} \tag{5}$$

where superscript β means the variables on the β th slip system; $\dot{\gamma}^{\beta}$ is the slip rate; and \mathbf{P}_S^{β} is the Schmid geometric projection tensor, calculated as the cross product of the plane normal \mathbf{n}^{β} and slip direction \mathbf{m}^{β} . According to the Orowan equation, $\dot{\gamma}^{\beta}$ depends on the mobile dislocation density ρ^{β} and dislocation velocity v^{β} , and is expressed as [20]

$$\dot{\gamma}^{\beta} = b \rho^{\beta} v^{\beta} \tag{6}$$

The motion of the screw dislocations and edge dislocations are dominated by the thermal-activated kink-pair mechanism and the phonon drag mechanism, respectively. The corresponding dislocation mobility laws have been established and expressed as [12,20]

$$v^{\beta}(\sigma, \theta) = \begin{cases} \frac{\tau_{eff}^{\beta} b}{B(\sigma, \theta)} \exp\left(-\frac{\Delta G_{kp}(\sigma, \theta)}{2k\theta}\right) & \text{if } \Delta G_{kp}(\sigma, \theta) > 0 \\ \frac{\tau_{eff}^{\beta} b}{B(\sigma, \theta)} & \text{if } \Delta G_{kp}(\sigma, \theta) \leq 0 \end{cases} \tag{7}$$

$$\Delta G_{kp}(\sigma, \theta) = \Delta H_0 \left\{ \left[1 - \left(\Theta^{\beta}(\sigma) \right)^{q_1} \right]^{q_2} - \frac{\theta}{\theta_A} \right\} \tag{8}$$

$$\Theta^{\beta}(\sigma) = \frac{\tau_{eff}^{\beta} + a_1 \sigma : (\mathbf{m}^{\beta} \otimes \mathbf{n}_1^{\beta})}{a_0 \tau_p - a_2 \sigma : ((\mathbf{n}^{\beta} \times \mathbf{m}^{\beta}) \otimes \mathbf{n}^{\beta}) - a_3 \sigma : ((\mathbf{n}_1^{\beta} \times \mathbf{m}^{\beta}) \otimes \mathbf{n}_1^{\beta})} \tag{9}$$

$$\sigma = J^{-1} \mathbf{F} \cdot \mathbf{S} \cdot \mathbf{F}^T \tag{10}$$

$$\mathbf{S} = \begin{cases} g(d) \mathbf{S}_0, & J \geq 1. \\ g(d) \mathbf{S}_0^{dev} + \mathbf{S}_0^{vol}, & J < 1. \end{cases} \tag{11}$$

where $\Delta G_{kp}(\sigma, \theta)$ is the activation enthalpy of the kink-pair depending on the Cauchy stress σ and the temperature θ [12], and considers the influence of the NS effect through the stress ratio $\Theta^{\beta}(\sigma)$. k is the Boltzmann’s constant; $B(\sigma, \theta)$ is the effective resistance

coefficient of dislocation motion; θ_A is the athermal transition temperature. $0 \leq q_1 \leq 1$ and $1 \leq q_2 \leq 2$ are the fitting parameters; the unit vector n_1^β forms an angle of -60° with the β th slip plane. $a_0, a_1, a_2,$ and a_3 are the material-dependent constants and can be determined through atomistic calculations [12]. Among them, a_0 is related to the Schmid stress tensor and the resolved shear stress, and the remaining three parameters are related to the non-Schmid tensors concerning the twinning/anti-twinning asymmetry (T/AT) and the effects of the non-glide stress components [20]. F is the total deformation gradient, and F^T is the transpose of F . S is the second Piola–Kirchhoff stress of the damaged material, and calculated from the original stress S_0 of the undamaged material and the degeneration function $g(d)$. S_0^{dev} and S_0^{vol} are the deviatoric and volumetric part of S_0 , respectively. After the determination of σ (or resolved shear stress τ_{res}^β) and obstacle stress τ_{obs}^β , the effective shear stress τ_{eff}^β is calculated as

$$\tau_{eff}^\beta = \sigma : P_S^\beta - \tau_{obs}^\beta = \tau_{res}^\beta - \alpha_d \mu b \sqrt{\sum_{\beta=1}^{NS} \rho^\beta} \quad (12)$$

Note that τ_{obs}^β considers the dislocation forest hardening and is related to the number of considered slip systems NS , and the hardening coefficients α_d . μ is the shear modulus.

Considering the generation and annihilation process of the dislocations, the evolution of dislocation density $\dot{\rho}^\beta$ can be calculated as [40,41]

$$\dot{\rho}^\beta = \left(k_1 \sqrt{\rho^\beta} - k_2 (\dot{\epsilon}, \theta) \rho^\beta \right) \dot{\gamma} \quad (13)$$

where k_1, k_2 are the generation and annihilation coefficients of the dislocations, respectively.

The CP-PFM model has been carefully validated in our previous work [36], which can well capture the fracture behavior of a tungsten single crystal during the brittle–ductile transition (BDT) process from 77 K to 800 K. The predicted mechanical response agreed well with the experimental data, and the observed fracture morphologies were accurately simulated [5,42,43]. Therefore, the CP-PFM model and the corresponding material parameters in our previous work [36] were adopted to reveal the underlying mechanism of the NS effect influencing the fracture behavior of tungsten in the current work.

3. Non-Schmid Effect on the Plastic Deformation of Tungsten

The first question we wanted to explore was how the NS effect influences the plastic deformation in tungsten at different temperatures. To eliminate the influence of the material damage evolution, the CP part of the CP-PFM model was only adopted in this section to simulate the plastic deformation of tungsten under the two conditions, namely, with and without the NS effect. This CP model has been carefully validated and applied to predict the temperature-dependence and loading-orientation dependence of the mechanical response for tungsten in our previous work [17,44]. Cylindrical dog-bone shaped single-crystal tungsten specimens were used to minimize the boundary effect, and uniaxial loading was applied at one end, as shown in Figure 1a. The diameter and length were 30 μm and 60 μm , respectively. The middle part of these specimens was meshed with the element size of 500 nm, and the mesh convergence was verified. The loading orientation was along [110]. The strain rate was about 0.05/s, and the temperature ranged from 150 K to 573 K.

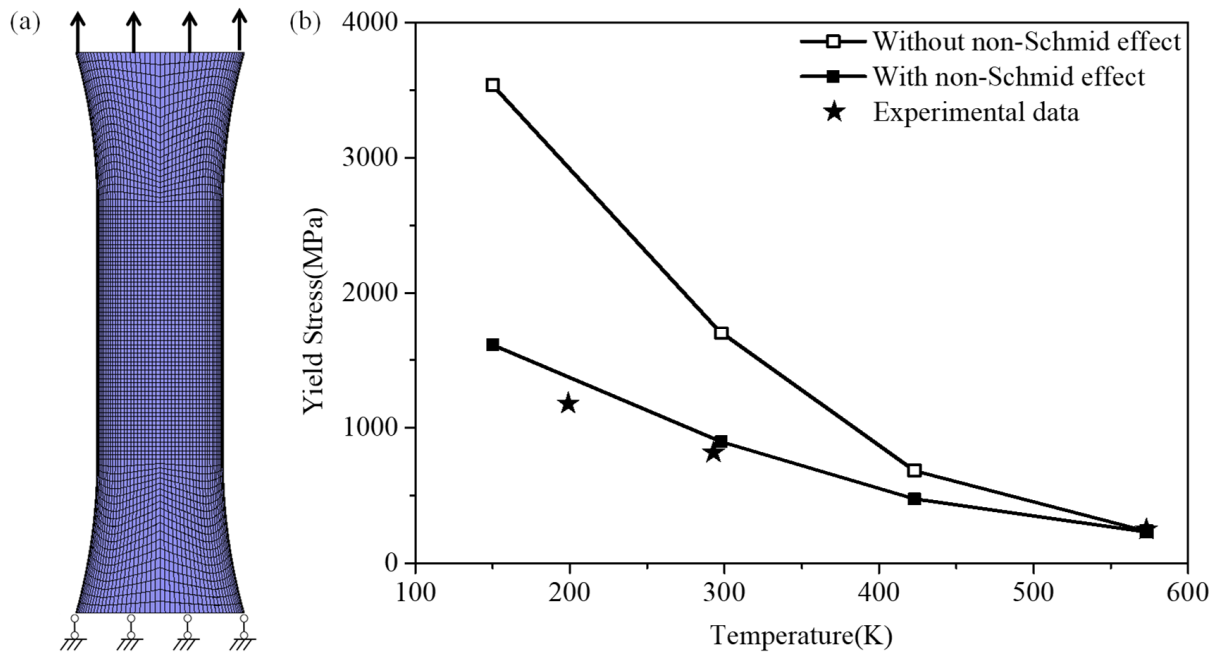


Figure 1. The NS effect on the yield stress of tungsten at different temperatures. (a) Boundary condition of the cylindrical dog-bone shaped specimen. (b) Predicted yield stress under the two conditions and the experimental data from [45,46].

Figure 1b shows the influence of the NS effect on the predicted yield stress of tungsten at different temperatures. When the NS effect was considered, the predicted values agreed well with the experimental data. If this effect was not considered, the predicted yield stress was much higher in the low and medium temperature regimes, as shown in Figure 1b. The deviation in the yield stress with and without the NS effect decreased with the temperature. When the temperature was 573 K, there was almost no difference (see Figure 1b). According to the dislocation mobility laws (see Equations (7)–(11)), the NS effect considers the contribution of non-planar shear stress on the mobility of the screw dislocations. By not considering this effect, this contribution of the non-planar stress component was ignored, and the dislocation velocity was underestimated, thus leading to the much higher yield stress than the experimental data. With the increase in temperature, the mobility law of screw dislocations is prone to being similar to that of edge dislocations, so the NS effect has a gradually weaker effect on the screw dislocation motion and the predicted yield stress.

On the other hand, the NS effect also affected the uniformity of plastic deformation. The evolution of dislocation density in two active slip systems of $[\bar{1}11](\bar{1}01)$ and $[111](\bar{1}01)$ was taken as the example to illustrate this effect at temperatures of 295 K and 573 K. As shown in Figure 2, when the NS effect was not considered, these two active slip systems (with the same Schmid factor) had the same dislocation density evolution, contributing to the same plastic deformation while the NS effect led to different contributions of plastic deformation. The increase in the dislocation density in the slip system of $[\bar{1}11](\bar{1}01)$ was much faster than that of $[111](\bar{1}01)$. This great difference is a direct manifestation of the heterogeneity of plastic deformation, and the higher possibility of localized deformation. By comparing Figure 2a,b, it can be seen that the difference between $[\bar{1}11](\bar{1}01)$ and $[111](\bar{1}01)$ decreased when the temperature increased from 295 K to 573 K, indicating a weaker role of the NS effect in influencing plasticity at a higher temperature.

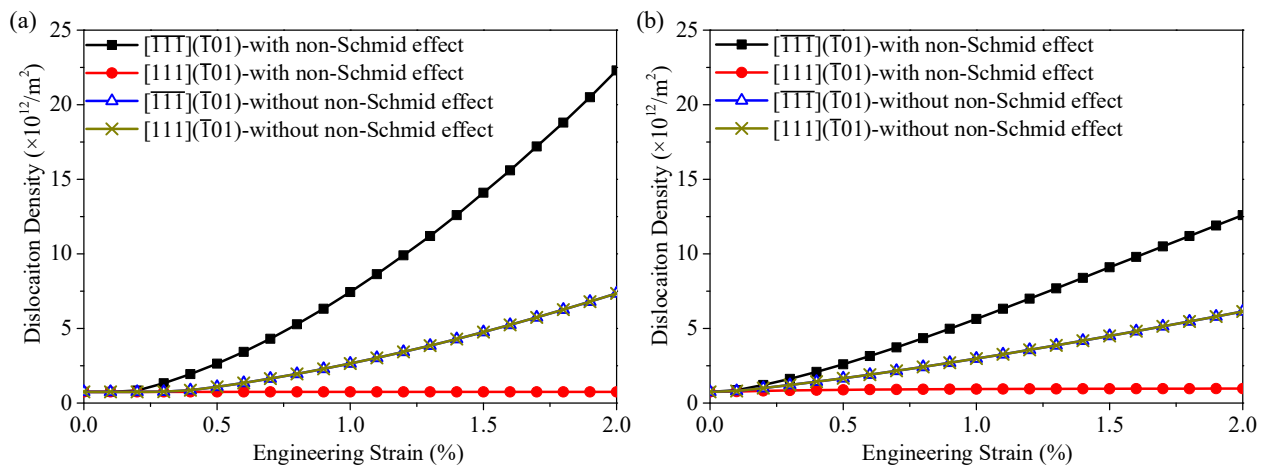


Figure 2. The NS effect on the dislocation density evolution of two typical slip systems at two different temperatures of (a) 295 K and (b) 573 K.

4. Non-Schmid Effect on the Fracture Behavior of Tungsten

The fracture behavior of tungsten is well-known to exhibit strong temperature dependence, which can be described as four typical fracture processes, namely, brittle fracture, semi-brittle fracture, micro-ductile fracture, and ductile fracture. These different fracture behaviors are induced by the competition between the plastic deformation and crack propagation, as discussed in detail in our previous work [36]. In the following, we will further explore how the NS effect influences the fracture behavior of tungsten.

A tensile load was applied on the top surface of a notched single crystal tungsten sample, and the bottom surface was constrained in the vertical direction, namely, the [010] direction, as schematically shown in Figure 3a. The corresponding tensile strain rate was about 0.04/s. The element size was about 200 nm in the pre-notched tip zone (see Figure 3b), and the critical plastic strain $\bar{\epsilon}_{p,lock}$ was set as 1.0. The plane strain model [36] was adopted, which can capture the fracture behavior of the tungsten sample [42] at a low computation cost. Five different temperatures were considered, namely, 77 K (low temperature, brittle fracture), 295 K (room temperature, semi-brittle fracture), 478 K and 550 K (medium temperature, micro-ductile fracture), and 800 K (high temperature, ductile fracture).

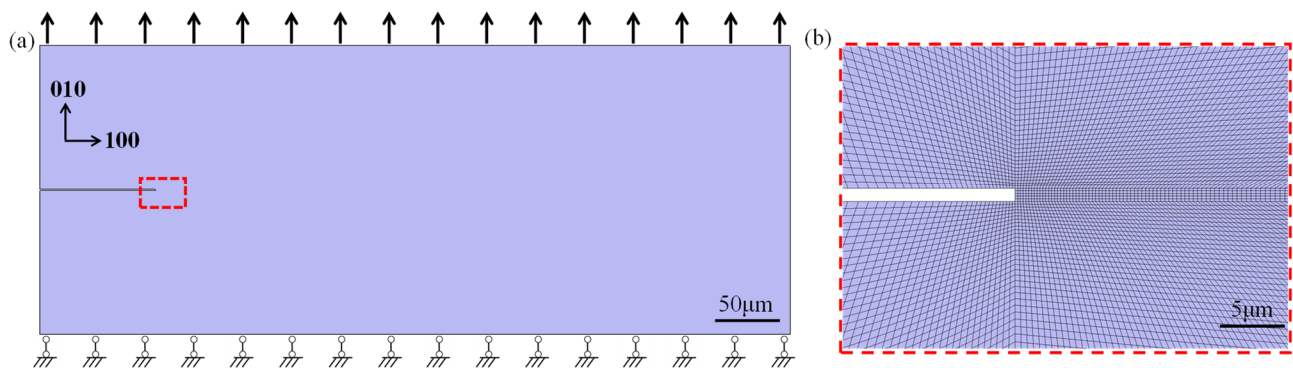


Figure 3. The notched single crystal tungsten sample. (a) The boundary conditions. (b) Enlargement of the mesh around the crack tip zone marked by the red dotted box in (a).

4.1. Mechanical Response

At first, we explored the influence of the NS effect on the mechanical response of the pre-notched tungsten samples during the crack propagation process. Figure 4 shows the engineering fracture stress and engineering fracture strain at five different temperatures under the two conditions of considering and ignoring the NS effect. In the current work,

the engineering fracture stress was defined as the maximum engineering stress during uniaxial tensile loading for the pre-notched sample, and the corresponding strain was defined as the engineering fracture strain. At 77 K, the dislocation motion was almost completely suppressed due to the lack of effective thermal activation, and the NS effect had no influence on the engineering fracture stress and engineering fracture strain of tungsten. For the highest temperature of 800 K, the thermal activation feature of dislocation mobility was weak. Therefore, the influence of the NS effect dramatically decreased, and the engineering fracture stress and fracture strain with and without the NS effect were basically the same. However, in the medium temperature regime (namely 295 K~550 K), there was obvious difference between the engineering fracture stresses (or fracture strains) with and without the NS effect for each temperature, as shown in Figure 4. In this temperature regime, the screw dislocation motion dominated the plastic deformation of tungsten, which was dominated by the kink-pair mechanism and noticeably affected by the NS effect. Ignoring the NS effect induced lower engineering fracture stress and engineering fracture strain for the pre-notched tungsten.

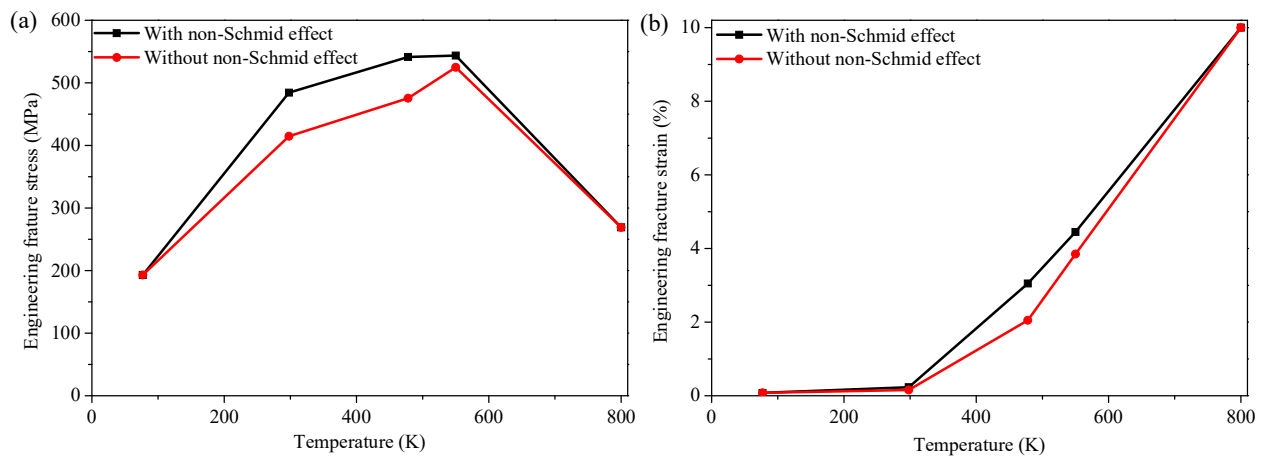


Figure 4. Influence of the NS effect on the engineering fracture stress (a) and engineering fracture strain (b) of tungsten at different temperatures.

4.2. Plastic Deformation near the Crack Tip

What is the underlying mechanism for the difference in the mechanical response considering and neglecting NS effect? To answer this question, the result at the temperature of 295 K was taken as an example to analyze the plastic deformation near the crack tip. Figure 5a,b,e,f shows the distribution of the equivalent plastic strain and the normal tensile stress for a given engineering strain of 0.15% under the two conditions, respectively. When the NS effect was considered, the equivalent plastic strain was larger than that without the NS effect, and the plastic zone size l_{pz} was also larger. For mode I fracture, l_{pz} along the crack propagation direction was inversely proportional to the square of yield stress σ_y , namely, $l_{pz} \propto 1/\sigma_y^2$ [36,47]. According to the simulation results in Section 3, neglecting the NS effect dramatically increased σ_y at room temperature (see Figure 1b), which induced the smaller plastic zone (or plastic shielding effect), as shown in Figure 5a,e. This great difference further led to the different distribution of the normal tensile stress (see Figure 5b,f) and damage state (see Figure 5c,g). The larger plastic zone (due to the NS effect), on one hand, reduced the absolute value of maximum tensile stress for a given engineering strain, and on the other hand, pushed forward the maximum tensile stress some distance away from the crack tip, which contributed to the larger engineering fracture stress and fracture strain.

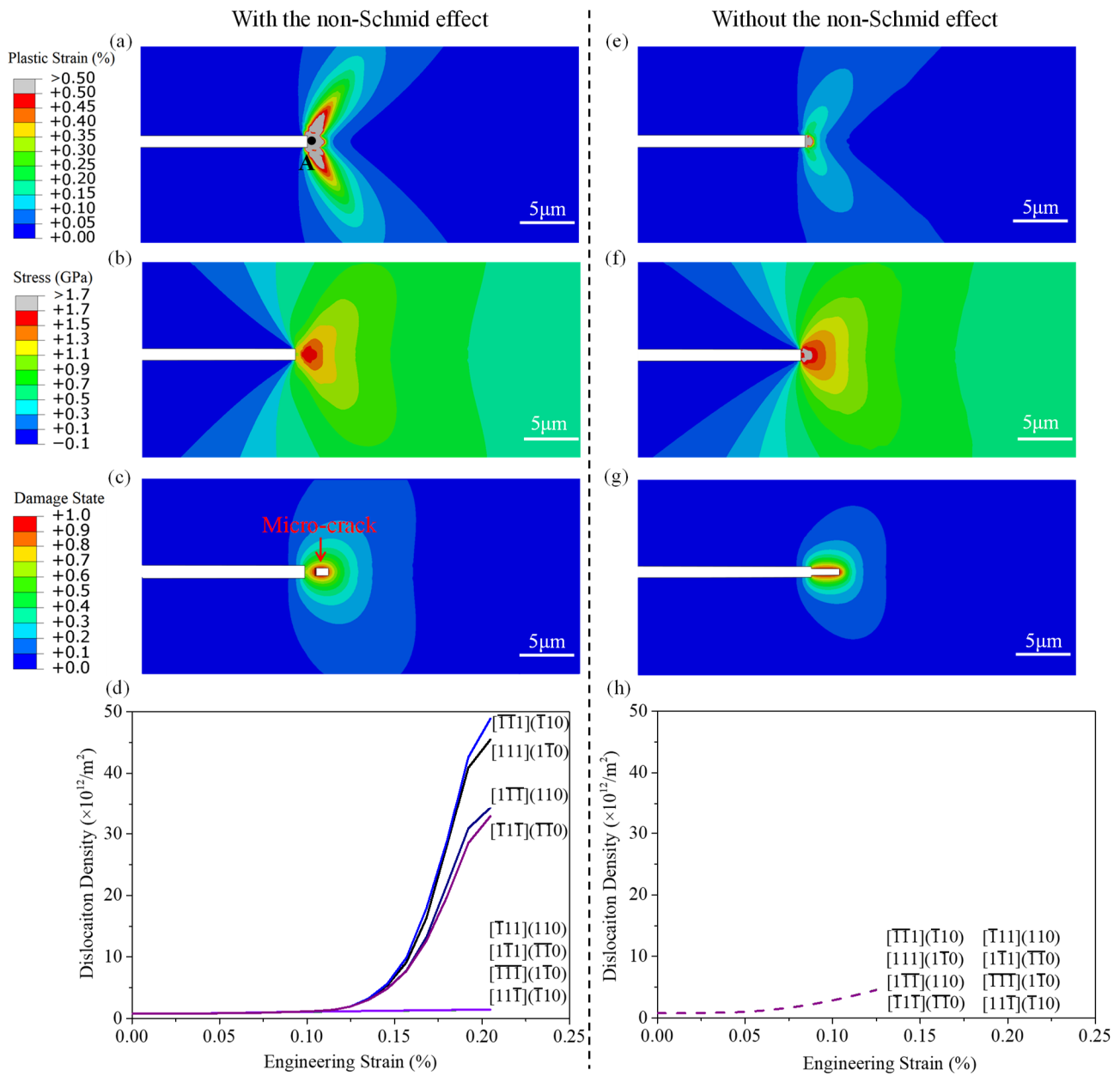


Figure 5. Distribution of equivalent plastic strain, normal tensile stress and damage state, and evolution of the dislocation density for the semi-brittle fracture of tungsten at 295 K. (a–d) considers the NS effect, while (e–h) neglects this effect. (a,e) are the distribution of equivalent plastic strain, while (b,f) are the distribution of normal tensile stress, when the engineering strain is 0.15%. (c,g) are the damage distribution during the crack initiation. (d,h) are the dislocation density evolution for a given position (marked with “A”) near the crack tip before the material is totally damaged (or the element is deleted).

We further explored how the NS effect influenced the dislocation motion of the main slip systems suffering from the complex stress state in the crack-tip zone. For a given position (marked with “A” in Figure 5a), the corresponding evolutions of dislocation density under the two conditions are shown in Figure 5d,h, respectively. Without considering the NS effect, the dislocation density evolutions of the eight main slip systems were the same (see Figure 5h). In contrast, these eight slip systems had significant different evolutions. The slip system of $[\overline{1}\overline{1}\overline{1}](1\overline{1}0)$, $[\overline{1}\overline{1}\overline{1}](\overline{1}10)$, $[\overline{1}\overline{1}\overline{1}](110)$, and $[\overline{1}\overline{1}\overline{1}](\overline{1}\overline{1}0)$ showed a much higher dislocation density than that of ignoring the NS effect and dominated the plastic

deformation. This is consistent with Section 3, as the NS effect breaks the homogeneity of plastic deformation near the crack tip.

4.3. Fracture Process

In this section, we further explore how the NS effect influences the fracture process of tungsten. Figure 6 shows the crack propagation of tungsten at different temperatures considering and neglecting the NS effect.

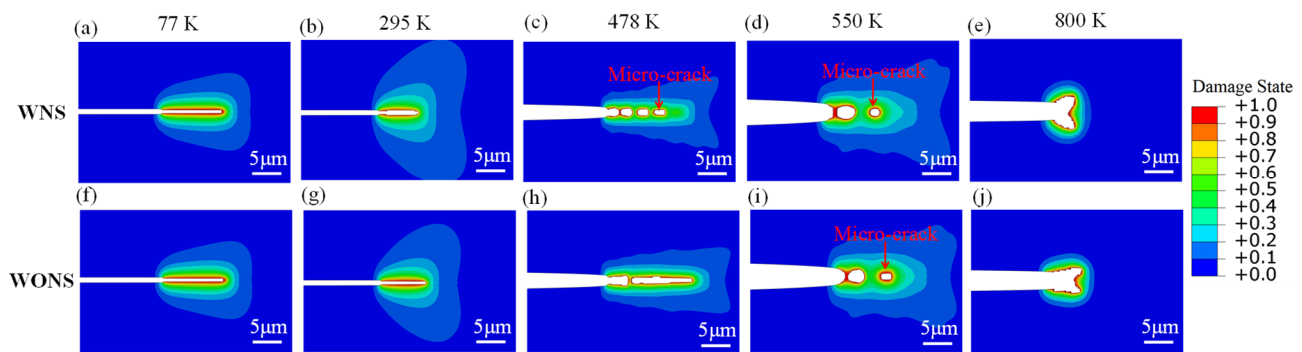


Figure 6. Crack propagation at different temperatures. (a–e) are the fracture processes with the NS effect, while (f–j) are the ones without the NS effect. Among them, (a,f) for 77 K and (g) for 295 K are the crack propagation of brittle fracture; (b) for 295 K and (h) for 478 K are the crack propagation of semi-brittle fracture; (c) for 478 K, (d,i) for 550 K are the crack propagation of micro-ductile fracture; (e,j) for 800 K are the crack propagation of ductile fracture, and a scale factor of 0.25 is applied to better present the deformation. “WNS” and “WONS” mean with and without the NS effect, respectively.

When the temperature was 77 K, brittle fracture occurred. The low temperature inhibited the motion of screw dislocation and the plastic deformation in the crack-tip zone. The crack initiated and then quickly propagated along the [010] crack plane, forming the smooth fracture surface. The process was not sensitive to the NS effect, as shown in Figure 6a,f.

At 295 K, when the NS effect was considered, a micro-crack first formed in the front of the pre-notched tip due to the shielding effect of the plastic zone, as shown in Figure 5a–c. This micro-crack expanded and connected to the pre-notched tip to form the main crack, and a small non-smooth fracture surface appeared near the pre-notched tip. After that, the main crack quickly propagated along the [010] crack plane, thus inducing a smooth fracture surface, as shown in Figure 6b. This fracture morphology agreed well with the experimental observations [42]. When the NS effect was neglected, tungsten suffered from brittle fracture without micro-cracks (see Figures 5g and 6g). This difference can be attributed to the different extents of plastic deformation in the crack-tip zone, as shown in Figure 7a. The NS effect promoted the development of the plastic zone, which provided a more effective shielding effect on the crack propagation.

At 478 K, a series of micro-cracks first nucleated and continuously expanded to form circular voids in front of the pre-notched tip, and then their connection led to slow crack propagation (see Figure 6c) when the NS effect was considered. The appearance and continuous growth of the micro-cracks can be attributed to the significant promotion of dislocation mobility at this higher temperature, which induced a stronger shielding effect on the propagation and connection of micro-cracks (see Figure 7b). Accordingly, the normal tensile stress (or the strain energy) was lower in the region between micro-cracks. The micro-crack collapse was only driven by severe plastic deformation, leading to the formation of micro-ductile fracture surfaces. The alternated micro-ductile fracture morphology and micro-cleavage fracture morphology (corresponding to micro-cracks) [36] have a width of about 2–3 μm , as marked by “*w*” and “*d*” in Figure 7b. This width was close to the distance of the fine striations (about 2 μm) observed in the experiment [42]. However, ignoring the

NS effect led to low dislocation mobility, and the plastic zone was much smaller near the first micro-crack and basically disappeared in the rest fracture surface region, as shown in Figure 7b. The fracture behavior became similar to the semi-brittle fracture, as shown in Figure 6h. During the crack initiation process, the plastic shielding effect was relatively strong (see Figure 7b), and the first micro-crack formed in front of the pre-notched tip. Once the main crack formed, the reduced shielding effect could not inhibit the cleavage crack propagation, which led to the formation of a smooth fracture surface (see Figure 6h).

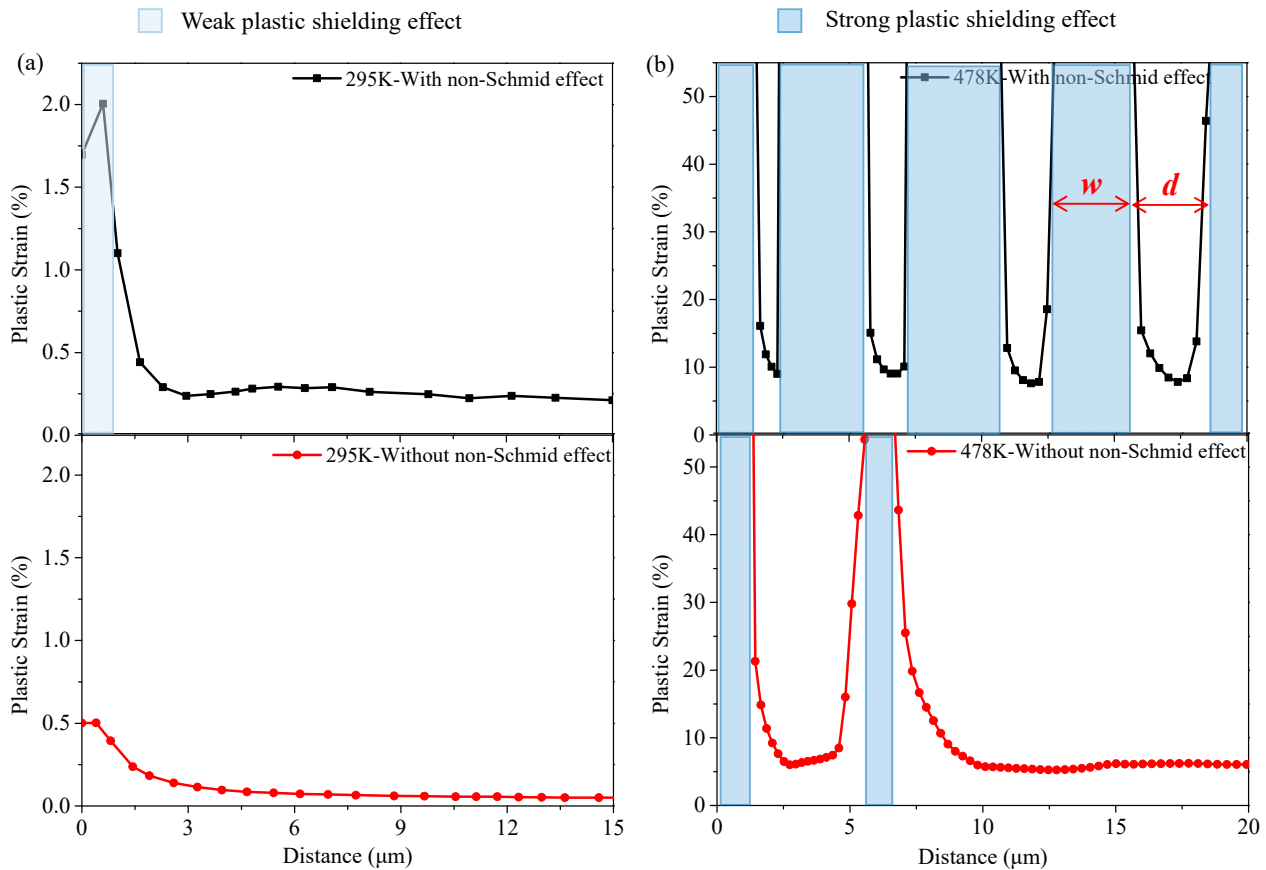


Figure 7. Influence of the NS effect on the plastic strain distribution along the crack plane for tungsten at two different temperatures of 295 K (a) and 478 K (b).

When the temperature increased to 550 K, the NS effect had a weaker effect on the fracture process of tungsten, and the two tungsten samples suffered from the micro-ductile fracture, as shown in Figure 6d,i. Note that the higher temperature of 550 K contributed to the larger distance between micro-cracks than that of 478 K by comparing Figure 6c,d.

At the high temperature of 800 K, the NS effect was weaker, as expected. Plastic deformation could well develop near the crack tip, contributing to a strong shielding effect. Whether the NS effect was considered or not, the main crack initiated from the pre-notched tip and then bifurcated (see Figure 6e,j).

4.4. Speed of Crack Propagation

Figure 8 shows the influence of the NS effect on the speed of crack propagation at different temperatures. The speed was calculated as the mean value during the initial 50 μm crack propagation distance from the pre-notched tip. During the micro-ductile fracture process, the newly formed micro-crack was taken as the crack tip when determining the crack propagation distance. To clearly show the NS effect, the speed ratio of the initial crack propagation was calculated as the ratio of the crack propagation speed without the NS effect to the one with this effect. At 77 K, the accumulated strain energy at the crack tip could

not be dissipated through the limited dislocation motion and plastic deformation. The increased strain energy quickly reached the threshold of the cleavage surface energy and contributed to a high speed of crack propagation. The NS effect led to a negligible difference (see Figure 8). With the increase in temperature, the higher plastic deformation contributed to more energy dissipation. Therefore, the speed of crack propagation decreased with the temperature (see Figure 8a). The NS effect noticeably promoted the plastic deformation and changed the fracture process at 295 K and 478 K (see Figure 6b,c,g,h). Neglecting the NS effect led to about a 30–80% increase in the speed of the initial crack propagation (see Figure 8b). When the temperature increased to 550 K, the difference in the crack propagation speed was smaller than 20%, as shown in Figure 8b.

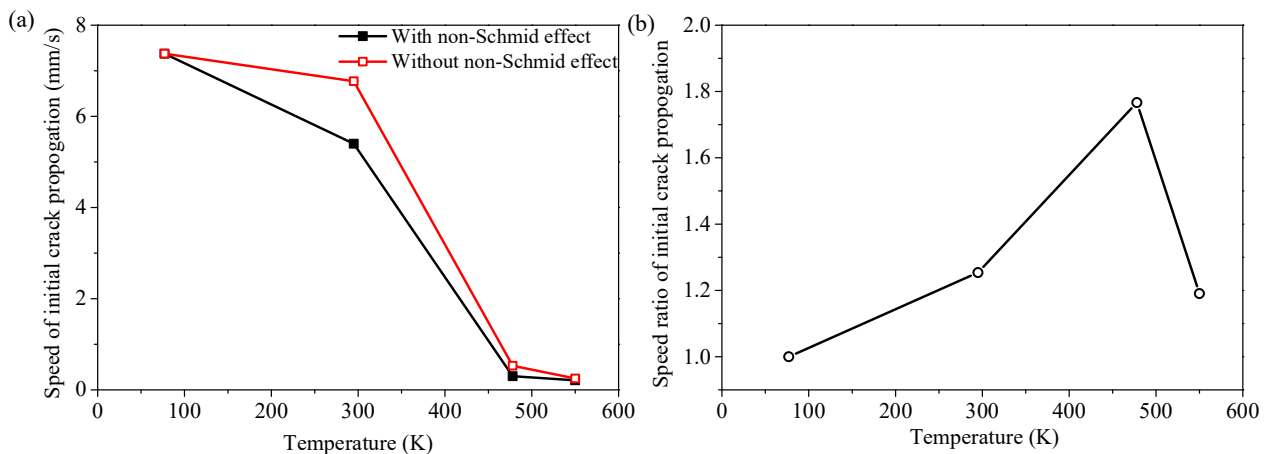


Figure 8. Influence of NS effect on the speed of crack propagation at different temperatures. (a) Speed of initial crack propagation from 77 K to 550 K. (b) Speed ratio of the initial crack propagation, which is the ratio of the initial crack propagation speed without the NS effect to the one with this effect and was calculated from (a).

5. Conclusions

In this work, the coupled crystal-plasticity and phase-field model (CP-PFM) was adopted to investigate the influence of the NS effect on the plastic deformation and the fracture process of tungsten at different temperatures. The following conclusions were gained.

The NS effect had the strongest effect on the plastic deformation of the un-notched tungsten at a lower temperature. Neglecting the NS effect will lead to a higher yield stress and more homogeneous plastic deformation.

The NS effect had the strongest effect on the fracture behavior of notched tungsten at a medium temperature. At low temperature, the brittle fracture occurred and the plastic deformation was neglected around the crack tip of tungsten, so the NS effect played almost no role. At high temperature (above $0.2 T_m$), the weak effect of the NS effect on plastic deformation further led to their weak effect on fracture behavior. Neglecting the NS effect will lead to lower fracture stress, a higher fracture propagation speed, more homogeneous plastic deformation around the crack tip, different fracture morphologies, and even a change in the fracture type at medium temperature.

Author Contributions: Conceptualization, Y.C.; formal analysis, Z.L.; methodology and investigation, Z.L. and Y.C.; writing—original draft preparation, Z.L.; writing—review and editing, Y.C. All authors have read and agreed to the published version of the manuscript.

Funding: This research was funded by National Natural Science Foundation of China (grant nos. 12102217, 11972208, and 12172194) and the Key R&D projects of the Ministry of Science and Technology (2022YFB4603000).

Data Availability Statement: Data are available upon request.

Acknowledgments: Our appreciation is expressed to Ronald W. Armstrong for the kind invitation.

Conflicts of Interest: The authors declare no conflict of interest.

References

1. Liu, J.; Barmak, K. Topologically close-packed phases: Deposition and formation mechanism of metastable β -W in thin films. *Acta Mater.* **2016**, *104*, 223–227. [[CrossRef](#)]
2. Costa, M.; Costa, A.T.; Hu, J.; Wu, R.Q.; Muniz, R.B. β -tungsten: A promising metal for spintronics. *J. Phys. Condens. Matter* **2018**, *30*, 305802. [[CrossRef](#)] [[PubMed](#)]
3. Abernethy, R.G.; Gibson, J.S.K.L.; Giannattasio, A.; Murphy, J.D.; Wouters, O.; Bradnam, S.; Packer, L.W.; Gilbert, M.R.; Klimenkov, M.; Rieth, M.; et al. Effects of neutron irradiation on the brittle to ductile transition in single crystal tungsten. *J. Nucl. Mater.* **2019**, *527*, 1–12. [[CrossRef](#)]
4. Linsmeier, C.; Rieth, M.; Aktaa, J.; Chikada, T.; Hoffmann, A.; Hoffmann, J.; Houben, A.; Kurishita, H.; Jin, X.; Li, M.; et al. Development of advanced high heat flux and plasma-facing materials. *Nucl. Fusion* **2017**, *57*, 092007. [[CrossRef](#)]
5. Yin, C.; Terentyev, D.; Pardo, T.; Petrov, R.; Tong, Z.F. Ductile to brittle transition in ITER specification tungsten assessed by combined fracture toughness and bending tests analysis. *Mater. Sci. Eng. A* **2019**, *750*, 20–30. [[CrossRef](#)]
6. Prakash, C.; Lee, H.; Alucozai, M.; Tomar, V. An analysis of the influence of grain boundary strength on microstructure dependent fracture in polycrystalline tungsten. *Int. J. Fract.* **2016**, *199*, 1–20. [[CrossRef](#)]
7. Rupp, D.; Weygand, S.M. Anisotropic fracture behaviour and brittle-to-ductile transition of polycrystalline tungsten. *Philos. Mag.* **2010**, *90*, 4055–4069. [[CrossRef](#)]
8. Giannattasio, A.; Roberts, S.G. Strain-rate dependence of the brittle-to-ductile transition temperature in tungsten. *Philos. Mag.* **2007**, *87*, 2589–2598. [[CrossRef](#)]
9. Bonnekoh, C.; Reiser, J.; Hartmaier, A.; Bonk, S.; Hoffmann, A.; Rieth, M. The brittle-to-ductile transition in cold-rolled tungsten sheets: The rate-limiting mechanism of plasticity controlling the BDT in ultrafine-grained tungsten. *J. Mater. Sci.* **2020**, *55*, 12314–12337. [[CrossRef](#)]
10. Gröger, R.; Bailey, A.; Vitek, V. Multiscale modeling of plastic deformation of molybdenum and tungsten: I. Atomistic studies of the core structure and glide of $1/2\langle 111 \rangle$ screw dislocations at 0 K. *Acta Mater.* **2008**, *56*, 5401–5411.
11. Gröger, R.; Racherla, V.; Bassani, J.; Vitek, V. Multiscale modeling of plastic deformation of molybdenum and tungsten: II. Yield criterion for single crystals based on atomistic studies of glide of $1/2\langle 111 \rangle$ screw dislocations. *Acta Mater.* **2008**, *56*, 5412–5425.
12. Po, G.; Cui, Y.N.; Rivera, D.; Cereceda, D.; Swinburne, T.D.; Marian, J.; Ghoniem, N. A phenomenological dislocation mobility law for bcc metals. *Acta Mater.* **2016**, *119*, 123–135. [[CrossRef](#)]
13. Knezevic, M.; Beyerlein, I.J.; Lovato, M.L.; Tomé, C.N.; Richards, A.W.; McCabe, R.J. A strain-rate and temperature dependent constitutive model for BCC metals incorporating non-Schmid effects: Application to tantalum–tungsten alloys. *Int. J. Plast.* **2014**, *62*, 93–104. [[CrossRef](#)]
14. Weinberger, C.R.; Battaile, C.C.; Buchheit, T.E.; Holm, E.A. Incorporating atomistic data of lattice friction into BCC crystal plasticity models. *Int. J. Plast.* **2012**, *37*, 16–30. [[CrossRef](#)]
15. Lim, H.; Hale, L.M.; Zimmerman, J.A.; Battaile, C.C.; Weinberger, C.R. A multi-scale model of dislocation plasticity in α -Fe: Incorporating temperature, strain rate and non-Schmid effects. *Int. J. Plast.* **2015**, *73*, 100–118. [[CrossRef](#)]
16. Lim, H.; Weinberger, C.R.; Battaile, C.C.; Buchheit, T.E. Application of generalized non-Schmid yield law to low-temperature plasticity in bcc transition metals. *Model. Simul. Mater. Sci. Eng.* **2013**, *21*, 1–23. [[CrossRef](#)]
17. Li, Z.; Liu, Z.; Zhuang, Z.; Cui, Y. Temperature dependent deformation localization in irradiated tungsten. *Int. J. Plast.* **2021**, *146*, 103077. [[CrossRef](#)]
18. Qin, Q.; Bassani, J.L. Non-associated plastic flow in single crystals. *J. Mech. Phys. Solids* **1992**, *40*, 835–862. [[CrossRef](#)]
19. Steinmann, P.; Kuhl, E.; Stein, E. Aspects of non-associated single crystal plasticity: Influence of non-Schmid effects and localization analysis. *Int. J. Solids Struct.* **1998**, *35*, 4437–4456. [[CrossRef](#)]
20. Cereceda, D.; Diehl, M.; Roters, F.; Raabe, D.; Perlado, J.M.; Marian, J. Unraveling the temperature dependence of the yield strength in single-crystal tungsten using atomistically-informed crystal plasticity calculations. *Int. J. Plast.* **2016**, *78*, 242–265. [[CrossRef](#)]
21. Bohnert, C.; Schmitt, N.J.; Weygand, S.M.; Kraft, O.; Schwaiger, R. Fracture toughness characterization of single-crystalline tungsten using notched micro-cantilever specimens. *Int. J. Plast.* **2016**, *81*, 1–17. [[CrossRef](#)]
22. Bohnert, C.; Weygand, S.M.; Schmitt, N.J.; Schwaiger, R.; Kraft, O. Orientation dependence of the fracture behavior of single-crystal tungsten. *Proc. Mat. Sci.* **2014**, *3*, 479–484. [[CrossRef](#)]
23. Vogler, T.J.; Clayton, J.D. Heterogeneous deformation and spall of an extruded tungsten alloy: Plate impact experiments and crystal plasticity modeling. *J. Mech. Phys. Solids* **2008**, *56*, 297–335. [[CrossRef](#)]
24. Cheng, J.; Tu, X.; Ghosh, S. Wavelet-enriched adaptive hierarchical FE model for coupled crystal plasticity-phase field modeling of crack propagation in polycrystalline microstructures. *Comput. Methods Appl. Mech. Eng.* **2020**, *361*, 112757. [[CrossRef](#)]
25. Ambati, M.; Gerasimov, T.; De Lorenzis, L. A review on phase-field models of brittle fracture and a new fast hybrid formulation. *Comput. Mech.* **2015**, *55*, 383–405. [[CrossRef](#)]
26. Clayton, J.; Knap, J.J.C.M.S. Phase field modeling of directional fracture in anisotropic polycrystals. *Comput. Mater. Sci.* **2015**, *98*, 158–169. [[CrossRef](#)]

27. McAuliffe, C.; Waisman, H. A coupled phase field shear band model for ductile–brittle transition in notched plate impacts. *Comput. Methods Appl. Mech. Eng.* **2016**, *305*, 173–195. [[CrossRef](#)]
28. Miehe, C.; Dal, H.; Schänzel, L.M.; Raina, A. A phase-field model for chemo-mechanical induced fracture in lithium-ion battery electrode particles. *Int. J. Numer. Methods Eng.* **2016**, *106*, 683–711. [[CrossRef](#)]
29. Shen, R.L.; Waisman, H.; Guo, L.C. Fracture of viscoelastic solids modeled with a modified phase field method. *Comput. Methods Appl. Mech. Eng.* **2019**, *346*, 862–890. [[CrossRef](#)]
30. Navidtehrani, Y.; Betegón, C.; Martínez-Pañeda, E. A simple and robust Abaqus implementation of the phase field fracture method. *Appl. Eng. Sci.* **2021**, *6*, 100050. [[CrossRef](#)]
31. Shanthraj, P.; Svendsen, B.; Sharma, L.; Roters, F.; Raabe, D. Elasto-viscoplastic phase field modelling of anisotropic cleavage fracture. *J. Mech. Phys. Solids* **2017**, *99*, 19–34. [[CrossRef](#)]
32. De Lorenzis, L.; McBride, A.; Reddy, B.D. Phase-field modelling of fracture in single crystal plasticity. *GAMM-Mitteilungen* **2016**, *39*, 7–34. [[CrossRef](#)]
33. Diehl, M.; Wicke, M.; Shanthraj, P.; Roters, F.; Brueckner-Foit, A.; Raabe, D. Coupled Crystal Plasticity-Phase Field Fracture Simulation Study on Damage Evolution Around a Void: Pore Shape Versus Crystallographic Orientation. *JOM* **2017**, *69*, 872–878. [[CrossRef](#)]
34. Vrielink, M.O.; van Dommelen, J.; Geers, M.G. Computational analysis of the evolution of the brittle-to-ductile transition of tungsten under fusion conditions. *Model. Simul. Mater. Sci. Eng.* **2020**, *29*, 015005. [[CrossRef](#)]
35. Xiao, X.Z.; Terentyev, D.; Ruiz, A.; Zinovev, A.; Bakaev, A.; Zhurkin, E.E. High temperature nano-indentation of tungsten: Modelling and experimental validation. *Mat. Sci. Eng. A* **2019**, *743*, 106–113. [[CrossRef](#)]
36. Li, Z.; Wang, T.; Chu, D.Y.; Liu, Z.; Cui, Y. A coupled crystal-plasticity and phase-field model for understanding fracture behaviors of single crystal tungsten. *Int. J. Plast.* **2022**, *157*, 103375. [[CrossRef](#)]
37. Armstrong, R.W. Dislocation Mechanics Pile-Up and Thermal Activation Roles in Metal Plasticity and Fracturing. *Metals* **2019**, *9*, 154. [[CrossRef](#)]
38. Yu, Q.R.; Chatterjee, S.; Roche, K.J.; Po, G.; Marian, J. Coupling crystal plasticity and stochastic cluster dynamics models of irradiation damage in tungsten. *Model. Simul. Mater. Sci. Eng.* **2021**, *29*, 055021. [[CrossRef](#)]
39. Miehe, C.; Hofacker, M.; Schaanzenel, L.M.; Aldakheel, F. Phase field modeling of fracture in multi-physics problems. Part II. Coupled brittle-to-ductile failure criteria and crack propagation in thermo-elastic-plastic solids. *Comput. Methods Appl. Mech. Eng.* **2015**, *294*, 486–522. [[CrossRef](#)]
40. Beyerlein, I.J.; Tome, C.N. A dislocation-based constitutive law for pure Zr including temperature effects. *Int. J. Plast.* **2008**, *24*, 867–895. [[CrossRef](#)]
41. Terentyev, D.; Xiao, X.Z.; Dubinko, A.; Bakaeva, A.; Duan, H.L. Dislocation-mediated strain hardening in tungsten: Thermo-mechanical plasticity theory and experimental validation. *J. Mech. Phys. Solids* **2015**, *85*, 1–15. [[CrossRef](#)]
42. Hull, D.; Beardmore, P.; Valintine, A.P. Crack Propagation in Single Crystals of Tungsten. *Philos. Mag.* **1965**, *12*, 1021–1041. [[CrossRef](#)]
43. Shi, L.; Yu, J.; Cui, C.; Sun, X. Temperature dependence of deformation behavior in a Co–Al–W-base single crystal superalloy. *Mater. Sci. Eng. A* **2015**, *620*, 36–43. [[CrossRef](#)]
44. Li, Z.J.; Cui, Y.N. Influence of loading orientation on deformation localization of irradiated tungsten. *J. Nucl. Mater.* **2023**, *573*, 154112. [[CrossRef](#)]
45. Garrison, L.M.; Katoh, Y.; Kumar, N.A.P.K. Mechanical properties of single-crystal tungsten irradiated in a mixed spectrum fission reactor. *J. Nucl. Mater.* **2019**, *518*, 208–225. [[CrossRef](#)]
46. Argon, A.S.; Maloof, S.R. Plastic Deformation of Tungsten Single Crystals at Low Temperatures. *Acta Metall.* **1966**, *14*, 1449–1462. [[CrossRef](#)]
47. Pan, J.; Lin, S.-H. Fracture mechanics and fatigue crack propagation. In *Fatigue Testing Analysis*; Palgrave: London, UK, 2005; pp. 237–284.

Disclaimer/Publisher’s Note: The statements, opinions and data contained in all publications are solely those of the individual author(s) and contributor(s) and not of MDPI and/or the editor(s). MDPI and/or the editor(s) disclaim responsibility for any injury to people or property resulting from any ideas, methods, instructions or products referred to in the content.